



Real-Time Aerosol Optical Properties, Morphology and Mixing States under Clear, Haze and Fog Episodes in the Summer of Urban Beijing

4 Rui Li¹, Yunjie Hu¹, Ling Li¹, Hongbo Fu^{1,2,*}, Jianmin Chen^{1,*}

5 ¹ *Shanghai Key Laboratory of Atmospheric Particle Pollution and Prevention, Department of*
6 *Environmental Science & Engineering, Fudan University, Shanghai 200433, China Chinese*
7 *Academy of Sciences, Institute of Atmosphere Physics, Beijing 100029.*

8 ² Collaborative Innovation Center of Atmospheric Environment and Equipment Technology
9 (CICAEET), Nanjing University of Information Science and Technology, Nanjing 210044,
10 China

11 Abstract

12 Characteristics of aerosol optical properties, morphologies and their relationship were studied
13 in urban Beijing during the clear, haze and fog episodes, sampled from 24th May to 22nd Jun,
14 2012. Transmission Electron Microscope (TEM), a Cavity Ring Down Spectrometer (CRDS),
15 a nephelometer and an aethalometer were employed to investigate the corresponding changes
16 of the aerosol properties. Five episodes were categorised according to the meteorological
17 conditions, composition and optical variation. Results show the clear episode (EP-2 and EP-4)
18 featured as the low light extinction with less pollutants, which are mostly externally mixed.
19 Coarse particles were scarcely observed in EP-2 due to the washout of a previous heavy rain.
20 Thus the size distribution in EP-2 was smaller than EP-4, which had some mineral particles



22 induced haze (EP-5) were both impacted by the south air mass. Higher AOD (Aerosol Optical
23 Depth) values illustrated heavy loading particle concentrations. Due to the collision, size of
24 most particles was larger with the diameter of $1 \mu\text{m}$, resulting in a higher scattering coefficient.
25 However, as the influence of severe crop residue combustion, a large fraction of soot was
26 detected, which sticks to the KCl transformed sulphate or nitrate particles. The light absorption
27 enhancement was contributed by both Black Carbon (BC) acceleration and other light
28 absorbing substances. Comparatively, soot fog period detected in EP-3 was mostly internally
29 mixed with sulphates and nitrates, which revealed themselves after electron exposure. The
30 larger size distribution was likely to be caused by both hygroscopic growth and collision. More
31 internally mixed particles were observed, which favored the light absorption. The comparison
32 of all the episodes provides a deeper insight of how mixing states influence the aerosol
33 extinction properties and also a clue to the air pollution control in the crop burning seasons.

34 **Keywords:**

35 Aerosol optical depth, Ångström exponents, Single scattering albedo, Transmission Electron
36 Microscope, Biomass burning, Soot

37 **1. Introduction**

38 Aerosol particles are ubiquitous in the troposphere and exert an important influence on global
39 climate and the environment (Ramana et al., 2010). They affect climate through direct
40 scattering, transmission, and absorption of radiation, or indirectly by acting as nuclei for cloud
41 formation (Buseck and Posfai, 1999). In addition, light extinction by aerosol particles can



42 impair visibility, both during extreme events such as dust storms, and more widely in the
43 vicinity of urban regions, frequently leading to regional haze and fog events (Wang et al.,
44 2009a;Chameides et al., 1999;Sun et al., 2006). Common scattering aerosols in the atmosphere
45 include inorganic salts and light-color organic carbon. These aerosols have mainly a “cooling
46 effect” on the climate due to a decrease in the solar radiation that reaches the Earth’s surface
47 (Buseck and POsfai, 1999). Soot aerosols, mineral dust, and brown carbon are important
48 absorbing aerosols that can lead to global and regional warming effects (Buseck and POsfai,
49 1999;Bahadur et al., 2012;Wang et al., 2014). The impact of aerosols on the Earth’s climate is
50 a major uncertainty in climate change models as was emphasized in the latest
51 Intergovernmental Panel on Climate Change (IPCC) report (Solomon, 2007). It follows that
52 understanding aerosol optical behaviour and associated spatial and temporal variability is a
53 necessary prerequisite to understanding its role in climate and the environment (Langridge et
54 al., 2012;Che et al., 2014).

55 Soot is a major contributor to Earth’s radiative balance (Ramana et al., 2010). Recent
56 investigations involving direct atmospheric measurements of soot aerosols suggest that they
57 may have a global warming potential second only to CO₂, and the warming effect by soot nearly
58 balances the net cooling effect of other anthropogenic aerosols (Jacobson, 2001). Not
59 surprisingly, the importance of soot to climate change has been a major focus of many
60 modelling, laboratory, and field studies (Zhang et al., 2008;Adler et al., 2010;Moffet and
61 Prather, 2009;Adachi and Buseck, 2008;Ram et al., 2012). The main uncertainty stems from
62 the fact that the actual amount soot warms our atmosphere strongly depends on the manner and



63 degree in which it is mixed with other species, a property referred to as mixing state (Jacobson,
64 2001; Moffet and Prather, 2009). The mixing state was found to affect the soot global direct
65 forcing by a factor of 2.9. It has been shown that absorption by soot increases when soot
66 particles are internally mixed and/or coated with other less absorbing materials (Moffet and
67 Prather, 2009). This enhanced absorption in such structure is because of the lensing effect of
68 coated materials (Jacobson, 2001). Field measurements indicate that during transport from the
69 sources, fresh soot becomes internally mixed with sulphate and organics, leading to
70 enhancement in light absorption, which confirms the modelling calculation (Kleinman et al.,
71 2007; Doran et al., 2007; Carabali et al., 2012). Kleinman et al. observed a doubling in the ratio
72 of aerosol light absorption in aged air masses compared to fresh emissions over the eastern U.S.
73 (Kleinman et al., 2007). Similar increases in absorption by soot-bearing aerosol have been
74 reported from ground site measurements performed at a series of locations downwind of
75 Mexico City (Doran et al., 2007). Compiling both the surface and aircraft measurements,
76 Ramana et al. recommended that the solar-absorption efficiency of the Beijing and Shanghai
77 plumes was positively correlated with the ratio of soot to sulphate (Ramana et al., 2010). Lei et
78 al. further confirmed that the enhanced absorption of mixed aerosols depended upon
79 hygroscopicity and the thickness of the coating (Lei et al., 2014). Based on the combined proof
80 from the modelling and field studies, most of researchers proposed that internal mixing models
81 of soot present more realistic absorption estimates as compared to external mixing models in
82 which soot particles coexist with other particles in a physically separated manner (Jacobson,
83 2001; Ramana et al., 2010; Lei et al., 2014).



84 Biomass burning is by far the largest source of primary, fine carbonaceous aerosols in the
85 atmosphere (Habib et al., 2008). It is estimated to contribute 20% of soot aerosols from biomass
86 burning. Besides strongly absorbing soot particles, high amounts of brown organic carbon, such
87 as “tar ball” or HULIS, can be emitted from biomass burning (Roden et al., 2006; Hand et al.,
88 2005; Hoffer et al., 2006). Brown carbon has a significant absorbing component at short
89 wavelengths that may be comparable to the soot absorption (Alexander et al., 2008; Bahadur et
90 al., 2012). Consequently, organic carbon from biomass burning may also contribute to the
91 warming potential of aerosols (Alexander et al., 2008). These large quantities of climate-related
92 aerosols can persist in the atmosphere for several weeks and be transported over long distances.
93 As a result, biomass burning aerosols have a significant impact on climate, which was
94 considered to provide a major uncertainty in accurately predicting the effects of light-absorbing
95 aerosols on the climate (Bahadur et al., 2012). Many field measurements in East Asia, South
96 Asia and Africa have shown extensive biomass burning in these regions causes important
97 perturbations to Earth’s atmosphere (Gustafsson et al., 2009; Alexander et al., 2008; Hand et
98 al., 2005). Once biomass burning particles are mixed with other atmospheric components
99 during aging and transport, such as sulfate and dust, solar absorption is further amplified due
100 to the formation of internally mixed particles (Ramanathan et al., 2005). Such mixtures of
101 absorbing and scattering aerosols at the regional scale are referred to as ABCs, for atmospheric
102 brown clouds (Ramanathan et al., 2007). ABCs radiative forcing can cool the surface, stabilize
103 the atmosphere, and reduce evaporation and monsoonal rainfall. The large influence of ABCs



104 on the climate and hydrological cycle changes has recently been demonstrated through model
105 simulations (Ramanathan et al., 2007; Ramanathan et al., 2005).
106 In the farmlands of eastern China such as that near Beijing, most wheat straw is burned in
107 the field within one week after harvesting in preparation for rice cultivation during May and
108 June. Emissions from the biomass burning are often transported and mixed with urban pollution,
109 leading to degradation of air quality, visibility impairment, and regional haze events (Li et al.,
110 2010). Stagnation occurs during episodes of urban haze, when there is insufficient wind
111 velocity to carry pollutants away from the city (Katrınak et al., 1993; Sun et al., 2006). During
112 these periods of pollutant retention, haze particles aggregate continue to collide and combine,
113 resulting in larger average sizes and altered morphology (Li et al., 2010). Enhanced absorption
114 is mainly brought about in the presence of high levels of non-absorbing hygroscopic aerosols
115 such as sulphates, nitrates, and water-soluble organic carbon, as their hygroscopic nature favors
116 internal mixing/core-shell formation (Bahadur et al., 2012). On the other hand, under the
117 condition of high atmospheric relative humidity (RH), the initially hydrophobic soot particles
118 can become associated with hygroscopic materials, leading to increased scattering due to
119 particle growth. At an extreme case, the coating material can cause the absorbing fractal soot
120 to collapse, potentially changing optical behaviour, to further complicate this picture (Zhang et
121 al., 2008; Langridge et al., 2012; Lei et al., 2014). Such changes cause both positive and
122 negative effects on the interplay between the direct and indirect aerosol effects, making overall
123 prediction of the radiative forcing difficult. Up to date, large uncertainties exist in estimates of
124 the radiative forcing of haze particles because of the lack of detailed in situ measurements of



125 the mixing state and the associated optical properties as a function of particle size and
126 composition (Moffet and Prather, 2009). These uncertainties limit our ability to quantify the
127 relative impacts of soot on climate, thus limiting our ability to make effective policy decisions.
128 In an attempt to address this knowledge gap, and in the absence of the opportunity for
129 widespread field studies in eastern China, the experiments in this study were designed to
130 simultaneously measure mixing states and optical properties of haze particles. The present
131 analysis focused on the Beijing plume, which in addition to strong urban emissions is
132 influenced by local agricultural emissions (Li et al., 2010). Light extinction and scattering
133 coefficient was measure with a cavity ring-down spectrometer (CRDs) and a nephelometer,
134 respectively. Absorption was calculated from the difference between extinction and scattering.
135 Individual aerosol particles were identified with transmission electron microscopy (TEM).
136 Back trajectory analyses suggest flow patterns consistent with long-range transport of
137 agricultural smoke to the study site during periods when the sampling site was engulfed by the
138 serious haze and fog.

139 **2. Experimental Sections.**

140 **2.1 site description**

141 All ambient investigation of aerosol optical properties and TEM samplings were conducted
142 at the Institution of Atmospheric Physics (39°58'N, 116°22'N), Beijing, China, from 24th May
143 to 22nd Jun, 2012. Samplers were mounted on the roof of a two-story building about 8 m above
144 ground level. The surroundings are in the convergence of residential and commercial zones
145 with some steel plants locating around in a distance of 6 to 25 km and a waste incineration



146 facility (Gaodun) 8 km in the northeast, which has an operational capacity of 1600 t d⁻¹. In
147 addition, the sampling site is suited in the middle of the North Third Ring Road and North
148 Fourth Ring Road, approximately 360 m south and 380 m north, respectively. The sampling
149 site is impacted by the mixture of residential, industrial, waste combustion and vehicle
150 emissions, but not dominated by any one source.

151 **2.2 Cavity ring-down spectrometer and nephelometer**

152 A self-designed cavity ring-down spectrometer (CRDS) is performed to measure the
153 extinction coefficient of aerosols at 1 min intervals with an accuracy of 0.1 Mm⁻¹. Aerosols
154 were dried by diffusion drying tubes before they reached the CRDS and Nephelometer to
155 exclude the influence of Relative humidity (RH) on the aerosol optical properties. RH is kept
156 below 40% to minimize the effects of changing RH on measurements. The cavity is formed by
157 two high-reflectivity dielectric mirrors (Los Gatos Research, Inc., Mountain View, CA, USA)
158 and a stainless steel cell equipped with two inlets at both ends and one outlet in the middle. The
159 entire distance of two mirrors is 76.4 cm, while the filling length is 58.0 cm. Dry nitrogen is
160 released near the mirrors at a flow of 0.03 L min⁻¹ to prevent the contamination of mirrors and
161 aerosol flow is set 1.0 L min⁻¹. The 532 nm light pulse (energy 100 μ J, duration 11 ns) is
162 generated by a Q-switched pulsed laser (CrystaLaser QG-532-500). Leaking light through the
163 mirrors is monitored by a Hamamatsu R928 photomultiplier. Details about the system were
164 reported by Li et al (2011). To calculate the decay time, 1000 ring-down traces are averaged at
165 1000 Hz repetition rate. The extinction coefficient (α_{ext}) has an uncertainty below 3% under
166 the controlled conditions. It is calculated according to the following equation:



167

$$\alpha_{ext} = \frac{L}{lc} \left(\frac{1}{\tau} - \frac{1}{\tau_0} \right) \quad (1)$$

168 Where L is the length of the cavity, l is effective length occupied by particles, c is the speed of light, τ_0
169 is ring-time time of the cavity filled with particle-free air and τ is the calculated decay time (Li et al.,
170 2011).

171 An integrating nephelometer (TSI, Model 3563) is operated to obtain aerosol scattering coefficient at three
172 different wavelengths (450, 550, and 700 nm) and the flow rate is set at 5 L min⁻¹. During the field campaign,
173 zero check is done automatically by pumping in particle-free air for 5 min once every 2 h, and a span check
174 is conducted manually using CO₂ as the high span gas and filtered air as the low span gas every week. RH
175 is kept below 40% to minimize the effects of changing RH on measurements (Peppler et al., 2000; Clarke
176 et al., 2007). The raw data were corrected for truncation errors and a non-Lambertian light source using
177 Ångström exponents (Å) according to Anderson and Ogren (1998) (Anderson and Ogren, 1998). Generally,
178 the total uncertainty of the scattering coefficient (α_{scat}) is generally below 10%. In accordance with the
179 extinction coefficient at 532 nm, the scattering coefficients is converted to 532 nm
180 ($\alpha_{scat,532}$) on the basis of the following equation:

181

$$\alpha_{scat,532} = \alpha_{scat,\lambda} \left(\frac{532}{\lambda} \right)^{-a} \quad (2)$$

182 Where $\alpha_{scat,\lambda}$ is the scattering coefficient at the wavelength of λ . Accordingly, Å can be computed
183 calculated as the equation (3),

184

$$a = - \frac{\lg(\alpha_{scat,\lambda_1} / \alpha_{scat,\lambda_2})}{\lg(\lambda_1 / \lambda_2)} \quad (3)$$

185 and the single scattering albedo (ω_0) at the given wavelength can be calculated from equation (4),

186

$$\omega_0 = \frac{\alpha_{scat}}{\alpha_{ext}} \quad (4)$$



187 As the sum of absorption (α_{abs}) and scattering (α_{scat}) coefficients equals the extinction coefficient (α_{ext}),

188 α_{abs} can be derived from the equation (5),

189
$$\alpha_{abs} = \alpha_{ext} - \alpha_{scat} \quad (5)$$

190 It is known that RH also has a profound impact on visibility (Chow et al., 2002), however, in this study the
191 aerosols passed through a diffusion drying tube before the measurement of optical properties, thus aerosol
192 optical property measurements and TEM observations were both performed in dry condition.

193 **2.3 Aethalometer**

194 An Aethalometer (model AE-31, Magee Scientific Company) was employed to simultaneously quantify
195 the black carbon (BC) concentration by calculating the optical attenuation (absorbance) of light from Light
196 Emitting Diode lamps emitting at seven different wavelengths (370, 470, 520, 590, 660, 880 and 950 nm)
197 every 5 minutes, with a typical half-width of 0.02 μm (Hansen, 2003). The flow rate was set to be 5 L min^{-1}
198 and a clean filter canister in the inlet was used weekly to conduct the zero calibration. A $\text{PM}_{2.5}$ cyclone
199 (BGI SCC 1.828) was employed in the sampling line with a flow rate of 5 L min^{-1} . A typical noise level is
200 less than 0.1 $\mu\text{g cm}^{-3}$ on a 5-min basis. Two photo-detectors monitor the light intensity as a function of time.
201 One measures the light intensity of the light crossing reference quartz filter, while the other measures that
202 of the same light crossing a sample spot under the identical conditions. The wavelength at 880 nm was used
203 to derive the aerosol absorption coefficient (σ_{abs}). Then BC concentration can be converted under the
204 assumption that the BC mass concentration [BC] on the filter is linearly correlated to the aerosol absorption
205 coefficient, as the following equation (6),

206
$$\sigma_{abs} = \alpha[BC] \quad (6)$$

207 Where [BC] is the BC mass concentration, and α is a conversion factor. A factor of $8.28 \text{ m}^2 \text{ g}^{-1}$ was
208 employed to convert the aerosol absorption coefficient to BC concentration, according to the results of
209 inter-comparison experiment conducted in south China (Wu et al., 2009; Yan et al., 2008).

210 The uncertainty of measurement might originate from the multiple scattering in the filter fibres in the
211 unloaded filter and in those particles embedded in the filters (Clarke et al., 2007; Jeong et al., 2004). The



212 attenuation values were within the limit of an acceptable uncertainty, that is, no greater than 150 in the
213 range of 75-125 at various wavelengths, verifying the reliability of the measurement. Moreover, the BC
214 concentration was compared with the results of multi-angle absorption photometry (MAAP, Model-5012)
215 and a particle soot absorption photometer (PSAP, Radiance Research), which shows great consistence.

216 **2.4 Aerosol optical depth**

217 Aerosol optical depth (AOD) data at the sampling site is based on the MODIS (Moderate Resolution
218 Imaging Spectroradiometer) retrieved data from a CIMEL CE-318 sunphotometer (AERONET/PHOTONS)
219 at Institute of Atmospheric Physics, reflecting the amount of direct sunlight prevented from reaching the
220 ground by aerosol particles by measuring the extinction of the solar beam. The AOD value of the sampling
221 site is downloaded from the AERONET (<http://aeronet.gsfc.nasa.gov>), using the Level 2.0. Quality Assured
222 Data. These data are pre and post field calibrated, automatically cloud cleared and manually inspected.
223 The regional distribution of AOD was obtained from Giovanni (GES-DISC Interactive Online Visualization
224 And Analysis Infrastructure) maps from MODIS satellite data (<http://disc.sci.gsfc.nasa.gov/giovanni>). Two
225 continuous episodes featuring as clear and haze are chosen, 23th May to 27th May and 19th June to 27th
226 June, respectively.

227 **2.5 TEM Analysis**

228 Samples were made by collecting air-borne particles onto copper TEM grids coated with carbon film
229 (carbon type-B, 300-mesh copper, Tianld Co., China) using a single-stage cascade impactor with a 0.5 mm
230 diameter jet nozzle at a flow rate of 1.0 L·min⁻¹. According to the visibility, the sampling time varies from
231 1 min to 10 min. 3 or 4 samples were collected each morning at around 8 am and also each time when haze
232 or fog appeared. After collection, samples were stored in a dry plastic box sealed in a plastic bag and kept
233 in a desiccator at 25 °C and 20 ± 3%. Details of the analysed samples, such as sampling time and
234 instantaneous meteorological state are listed in Table 1.

235 Individual aerosol samples were analysed using a high resolution TEM (JEOL 2010, Japan) operated at
236 200 kV. The TEM can obtain the morphology, size, and mixing state of individual aerosol particles. Energy-
237 dispersive X-ray spectrometer (EDS) can get the chemical compositions of the targeted particles. Cu and C



238 were excluded from the copper TEM grid with carbon film. Details can be found in our previous paper (Fu
239 et al., 2012; Guo et al., 2014a). Since particle sizes on the grid decrease from the centre to the periphery
240 due to the limitation of sampler, to ensure the representative of the entire size range, three to four round
241 meshes were chosen from the centre to the periphery in a line. Each mesh analyses three to four views. The
242 average values of each mesh were used for statistics. The analysis was done by labour-intensive manual
243 sortation of the particles. 9 grids, all together of 1173 particles have been analyzed by the TEM.

244 **2.6 Back trajectories and meteorological data**

245 NOAA/ARL Hybrid Single-Particle Lagrangian Integrated Trajectory model (available at
246 <http://www.arl.noaa.gov/ready/hysplit4.html>) was employed to determine back trajectories arriving at
247 Beijing at 100 m, employing the data of global data assimilation system (GDAS). Each trajectory
248 represented the past 72 h of the air mass, with its arrival time at 00:00 UTC every day.

249 Meteorological data was downloaded from Weather Underground (www.wunderground.com), and Daily
250 PM₁₀ values were transformed from daily API (Air Pollutant Index) in the datacentre of ministry of
251 Environmental Protection of the People's Republic of China (<http://datacenter.mep.gov.cn/>).

252 **3. Results and Discussion**

253 **3.1 Episodes segregations**

254 Haze is usually defined as a weather phenomenon that lasts a duration of at least 4 h when the visibility is
255 less than 10 km and RH lower than 80% (Sun et al., 2006), while fog is characterized with a higher RH,
256 larger than 90% in contrast, according to the Chinese Meteorological Administration. The sampling period
257 was categorized into 5 episodes to study the optical properties between different weather phenomena (Fig.
258 1). Although every episode contains a mixture of different pollutions, the main origin can be discerned by
259 studying the weather condition, back trajectories and fire maps. The 1st episode (EP-1) was from 28th May
260 to 29th May, when a haze occurred with the south wind bringing in the industrial pollution from the heavily
261 polluted cities in the south. This conformed to the 3-day back trajectories in Fig. 2a, showing the air masses
262 passing through Henan, Shandong, Hebei and Tianjin before arriving at the sampling site. Only scattered
263 fire spots were observed during these days along the air mass pathway, suggesting little biomass burning



264 emission interference. The 2nd episode (EP-2) was in clear weather on 30th May. A heavy rain interrupted
265 the previous haze; hence residuals were cleaned up by rain washout effect. It was impacted by the air mass
266 from the north region (Fig. 2b), as the north wind was relatively clean and the time was insufficient for a
267 heavy accumulation, this episode can be viewed as the background. The 3rd episode (EP-3) from 31st May
268 to 9th Jun was fickle, with a variety of transitions between fog, haze and clear days. This was partly caused
269 by the variable wind directions and air mass transferring (Fig. 2c). When the wind is from east side and the
270 back trajectories are across the Bohai Sea, the air mass carries a high content of water vapour, facilitating
271 the formation of fog, whereas when south wind is dominant, haze is likely to occur (Wang and Chen,
272 2014; Zhang et al., 2010). The following 4th episode (EP-4) from 10th Jun to 16th Jun was mainly clear days
273 with slight dust. Their back trajectories originated from the north part (Fig. 2d), mostly travelling from the
274 Siberian region, across eastern Mongolia and Inner Mongolia and arriving the site with little pollution but
275 a few dusts. The last episode (EP-5) was from 17th Jun to 21st Jun. Severe haze was observed in a long
276 duration. Together with the fire spots, Fig. 2e shows that the air parcel pathway across by dense fire spots,
277 indicating a severe impact of the biomass burning. Every year after harvest, crop residue burning is
278 extremely frequent in Anhui, Shandong and Henan provinces as they served as important centres for the
279 rice supply (Li et al., 2010)). Therefore, the biomass burning emissions can be the main contributor to the
280 haze formation in this episode. Besides the crop combustion, the high-loading fine metal particles observed
281 imply the influence of industrial sources.

282 **3.2 Optical parameter variation**

283 Aerosol optical depth (AOD) is representative of the airborne aerosol loading in the atmospheric column,
284 which is also verified by a significant related coefficient with PM₁₀ (R=0.603) (Fig. 1). The overall AOD
285 is contributed by both Mie scatter and Rayleigh scatter (Fig. 3a). The former one is produced by the scatter
286 effect of particles while the latter one by gases. Fig. 1 demonstrates that gas plays a negligible role in the
287 AOD value, especially when aerosol loading is high. Apparently, the AOD value varied with the weather
288 transition. During the clean days, the mean AOD was 0.723, while it became higher when the haze and fog



289 were formed, with a mean value of 2.92 and 1.14, respectively. Apart from the rain, AOD reached its highest
290 value of 5.0 in the hazy EP-5, which was more than 5 times than the average AOD of 0.95 in Beijing
291 measured from Mar 2012 to Feb 2013 (Guo et al., 2014b). Such high AOD could be attributed to the
292 pollutant accumulation, especially biomass burning emission from the crop combustion.

293 Ångström exponent (\AA) is a good indicator of aerosol size distribution, which decreases with the increase
294 of particle size (Eck et al., 1999). The value is computed from pairs of AOD measurements at 700 nm with
295 450 nm, 700 nm with 550 nm and 550 nm with 450 nm, respectively. A high accordance is observed
296 between each pair (Fig. 3b). The \AA increases sharply to its highest value above 2.0 at EP-2, 45 times of the
297 minimum value 0.044 observed in EP-5. This could be explained by the wet removal impact of the heavy
298 rain. It is well known that rains wash out the coarse particles, resulting in a fine size distribution (Dey et al.,
299 2004). The \AA value during EP-4 fluctuated between 0.08 and 0.2. Since the rains are light and short, the
300 clear days in EP-4 are more impacted by the north air mass, which brings in a larger fraction of coarse dust
301 particles. Comparatively, the \AA value was lower in both the haze and fog period including EP-1, EP-3 and
302 EP-5. Especially in the case of EP-5, the low \AA value indicated that the biomass burning emission could
303 contain more coarse particles. Such scene is in contrast to the conclusion that the haze days were dominated
304 by fine particles (Yan et al., 2008). It is likely caused by the high collision occurrences of fine particles
305 along the long-range transport from the fire spots (Wang et al., 2009b). In comparison, the \AA value during
306 2001 to 2005 in Beijing altered between 0.04 and 1.06 (Yu et al., 2006). The lower limit is similar with the
307 present field-measurement, while the upper limit is much higher than this study. This could be attributed to
308 the increase of fine particle emission contributed by more vehicles, waste incineration and industrial plants
309 during these years.

310 Single scattering albedo (SSA), ω , is defined as the ratio of the aerosol scattering coefficient (σ_{sca}) to the
311 extinction coefficient (σ_{ext}). This parameter is especially important in the estimation of direct aerosol
312 radiative forcing, since even a small error in its estimation might change the sign of aerosol radiative forcing
313 (Takemura et al., 2002). Figs. 3c and d show the time series of σ_{sca} , σ_{abs} , σ_{ext} and SSA at 550 nm during



314 the sampling period. The mean ω was 0.73, 0.82 and 0.79 in EP-2, EP-4, and EP-5, respectively, implying
315 that mineral dust in EP-4 accelerates the optical scattering while soot favours the optical absorption.
316 Compared with other reported results (Che et al., 2014; Li et al., 2007; Qian et al., 2007), the mean ω is
317 lower in this study, which supposed that more soot is presented. Research shows soot emission is much
318 higher in recent year, mainly contributed by the residential coal combustion, also biomass burning, coke
319 production, diesel vehicles and brick kilns (Wang et al., 2012b). Especially when air masses moved from
320 south direction to the sampling site aerosols were influenced by heavy soot-sulfate-OC-mixed pollution
321 from the dense population centres and industrial areas and substantial secondary aerosols are produced
322 during transport (Sun et al., 2006; Wang et al., 2006), which was also confirmed in the TEM observation.
323 In these conditions, SSA was even lower than those of the regions along the pathway.

324 **3.3 TEM analysis**

325 Based on morphology and chemical composition, we classified over 1173 particles into 9 categories: S-rich
326 (Fig. 4a), N-rich (Fig. 4b), mineral (Fig. 4c), K-rich (Fig. 4d), soot (Fig. 4e), tar ball (Fig.4f), organic
327 (Fig.4g), metal (Fig. 4h) and fly ash (Fig. 4i). The classification is similar to that adopted by Li Weijun (Li
328 and Shao, 2009).

329 The most common particles are sulphates and nitrates (Figs. 4a, b), which are of the size around 1.0
330 μm , and have a light scattering ability when externally mixed (Jacobson, 2001). Sulphates appeared as
331 subrounded masses under the TEM. They decomposed or evaporated under the electron beam exposure.
332 Conventionally, they were formed by the reaction of precursor SO_2 or H_2SO_4 with other gases or particles
333 (Khoder, 2002). Nitrates were mostly of scalloped morphology in the TEM view. They were relatively
334 stable when exposed to the electron beam. Nitrates formed through either the homogeneous reaction with
335 the precursor NO_2 or heterogenic reaction with HNO_3 (Khoder, 2002), but they possess a slower reaction
336 rate than sulphates. Thus, they usually follow the sulphate formation (Pathak et al., 2004; Seinfeld and
337 Pandis, 2012).

338 In the clear episodes influenced by the northern air mass, dust particles are relatively abundant. Dust
339 particles (Fig. 4c) were large in size, usually bigger than 1.0 μm , up to 8.0 μm under our sampling conditions.



340 Their compositions differed from each other, mostly are silicates and calcium sulphate or carbonate, which
341 were all stable to the electron beam. Dust particles were reported to have a light scattering effect, thus
342 resulting in negative aerosol radiative forcing (Wang et al., 2009b). They had a large portion in EP-4,
343 impacted by the north wind from the dusty regions.

344 As to the biomass burning related haze, notable tracer particles are presented, such as K-rich particles
345 (Li et al., 2010;Duan et al., 2004;Engling et al., 2009), soot (Li et al., 2010), tar ball (Chakrabarty et al.,
346 2010;Bond, 2001) and organic (Lack et al., 2012). K-rich particles (Fig. 4d) often exist as sulphate or nitrate.
347 A larger fraction of K-rich particles was found in the EP-5 than other periods. Together with the back
348 trajectories and fire spot maps, it further confirmed that the regional haze occurred in EP-5 was contributed
349 significantly by the field combustion. K-rich particles were characterized by the irregular shape which is
350 unstable when exposed to electron beam. KCl was barely detected in the samples, even though it has been
351 found to be internally mixed with K_2SO_4 and KNO_3 in fresh biomass burning plumes (Li et al., 2010;Li et
352 al., 2003;Adachi and Buseck, 2008). K-rich particles in our measurements showed that mostly they consist
353 of N, Na, O, S, and K and are free of Cl, implying KCl could have suffered from chemical reactions and
354 changed into sulphates or nitrates (Li and Shao, 2010), thus displaying negative climate forcing under
355 externally mixed conditions.

356 Soot (Fig. 4e) is vital to light absorption, which can alter regional atmospheric stability and vertical
357 motions, as well as influence the large scale circulation and precipitation with significant regional climate
358 effects (Ramanathan et al., 2001;Jacobson, 2002). It is another indicator of biomass combustion with a
359 structure like onion ring, resembling a fractal long chain as agglomerates of small spherical monomers (Li
360 and Shao, 2009). The fresh soot was loose and externally mixed. However, after undergoing a long-range
361 transportation, it has become more compacted, with a slight increase of O concentration because of the
362 photochemistry (Stanmore et al., 2001). Meanwhile, soot generally attaches to other particles on the surface
363 or serves as the core for other particle formation as the result of its stable and insoluble nature.

364 Tar ball (Fig. 4f) is a spherical carbon ball with a small fraction of O. It was thought to origin from the
365 smouldering combustion and have strong absorption effects (Chakrabarty et al., 2010;Bond, 2001). Tar



366 balls constituted a large fraction of the fresh emitted wildfire carbonaceous particles (China et al.,
367 2013;Lack et al., 2012). But it was seldom found in our study, even in EP-5 when there was severe biomass
368 burning emission. This may be caused by the difference in burning species. Most are wheat and rice residues
369 in this study, which have relatively less tar ball emission. An indoor chamber combustion simulation of the
370 different crop residues was conducted in our lab and confirms the speculation.

371 Organic matter (Fig. 4g) is amorphous specie and have a low contrast under the TEM view, which is
372 stable with strong electron beam exposure. It can be traced to the direct emission such as biomass burning
373 (Lack et al., 2012), or the second reaction between the VOCs with ozone (Wang et al., 2012a). It can absorb
374 radiation in the low-visible and UV wavelengths (Chakrabarty et al., 2010;Clarke et al., 2007;Lewis et al.,
375 2008;Hoffer et al., 2006). In addition, when compassing soot as the core, organic matter can enhance
376 absorption by internal mixing (Adachi and Buseck, 2008).

377 For the common haze and fog episodes, the stagnated weather favors the accumulation of pollutants,
378 especially metal particles and fly ash. Metal particles (Fig. 4h) are generally round and stable under the
379 TEM view. Less optical properties are discussed about the metal particles. Details of the classification of
380 metal species and origins were reported by Hu et al. (Hu et al., 2015). Fly ash (Fig. 4i) was a dark sphere
381 with the diameter usually below 1 μ m. It is a common product of industrial activities in the northern China
382 (Shi et al., 2003). As the complex refractive index (CRI) indicates, metal oxide particles and fly ash can
383 scatter light, but the former has a weak absorption ability while the later has almost no light absorption
384 ability (Ebert et al., 2004).

385 Figure 5 shows percentage of the 9 components in clear, haze and fog episodes under external, internal
386 and adjacent states (partially internal). About 28% of particles were internally mixed in the foggy days,
387 while about 52% of particles exhibited external mixing state in clear days through TEM analysis. Haze and
388 fog episodes had a higher possibility of collision due to the heavy particle loading, leading to a higher
389 adjacent state percentage around 65%.

390 **3.4 Optical properties related to morphological of aerosols**



391 The differences of the particle morphologies under different weather conditions can be easily observed,
392 and the results are shown in Fig. 6. Due to the washout effect of the heavy rain, particles in the typical clear
393 period EP-2 were normally smaller in size under the TEM (Figs. 6a, b), verifying the larger Ångström
394 exponent. The coarse particles, such as dusts, were hardly observed, whereas a few K-rich particles were
395 detected, of which presented in small cubic shape. Such particles could be attributed to the near-by coal
396 combustion around the sampling site due to the slight fire spots presence. Besides, the cubic shape of K-
397 rich particles suggested they have not undergone long transportation or severe photochemical reaction.
398 Likewise, soot was generally less oxidized in the haze and fog periods, maintaining fractional and externally
399 mixed. As the result of the existence of uncovered and less soot, SSA was higher. Small metal particles and
400 amorphous Zn-particles dominated the fine particles, which were attributed to the industrial activity and
401 waste incineration (Choël et al., 2006; Moffet et al., 2008).
402 In the biomass burning induced EP-5, the increase in aerosol loading played a remarkable role in the
403 enhancement of scattering coefficient and decrease of visibility (Kang et al., 2013; Charlson et al.,
404 1987; Deng et al., 2008). Because of the high rate of aerosol collision, particles were larger than the clear
405 days under the TEM (Figs. 6c, d), leading to a smaller Ångström exponent. Nearly all the soot studied in
406 this condition was compact and adhesive. It is predominantly adjacent to K-rich particles, which were larger,
407 rounder or with an outlayer of high S concentration. Together with the soot association on the surface, they
408 were probably transported from the south crop residual burning places and undergo some chemical changes,
409 verifying the trajectories passing through intense fire spots. Due to the high concentration of soot, these
410 haze periods are characterized with a high absorption coefficient, which was in accordance with the results
411 displayed in the Figure 3.
412 The BC variation during the sampling period was illustrated in Fig. 7. The preliminary component of BC
413 can be viewed as the soot. High BC concentration was easily recognized in EP-5 with a mean value of
414 $12.8 \mu\text{g m}^{-3}$, while it is $1.04 \mu\text{g m}^{-3}$ during clear periods. The former was about 11.3 times higher than the
415 later. In comparison, absorption coefficient of the EP-5 (468.7 Mm^{-1}) was about 94.7 times of the EP-4 (1.3



416 Mm⁻¹), more than 8 times of the BC ratio. Models estimated an enhancement of BC forcing up to a factor
417 of 2.9 when BC is internally mixed with other aerosols, compared with externally mixed scenarios
418 (Jacobson, 2001), which was much lower than this case. Accordingly, other light absorbing substances may
419 contribute to the discrepancy. Brown carbon is an indispensable component of biomass burning, which has
420 a strong absorption ability as well (Hoffer et al., 2006; Andreae and Gelencsér, 2006). Other particles like
421 dust may also contribute to the over-enhanced absorption coefficient (Yang et al., 2009). Our observations
422 were accordant with that of radiative forcing from aerosols in regional hazes over northern China, which
423 shows that aerosol particles under hazy weather conditions generate a positive heating effect on the
424 atmospheric column (Wang et al., 2009b; Xia et al., 2006).

425 In foggy days, particles were also generally larger than the clear days in the TEM views (Figs. 6e, f),
426 resulted from the hydroscopic growth under the high relative humidity, as well as the collision among
427 overloading particles, which was likewise illustrated by the Ångström exponent. Consequently, the larger
428 particles enhance the scattering of sunlight, and lead to higher reduction of visibility (Quan et al., 2011).
429 Moreover, Chow et al., reported that the relative humidity (RH) also has a profound impact on visibility
430 (Chow et al., 2002a). Some fan-like nitrate particles have inclusions which may act as the growth cores or
431 be encompassed during the hydroscopic growth. Bian et al. (2009) reported that whenever the RH is
432 elevated, its importance to the AOD is substantially amplified if the particles are hygroscopic (Bian et al.,
433 2009). Li et al. (2010) found that soot particles became hydrophilic when they were coated with the water-
434 soluble compounds such as (NH₄)₂SO₄, NH₄HSO₄, KNO₃, K₂SO₄, or oxidized organic matter, implying
435 that soot can provide important nuclei for the development of fine particles (Li et al., 2010). Furthermore,
436 Fig. 6e and 6f also illustrate a large fraction of internally mixed soot. It was not visible until being exposed
437 to electron beam for about 30 s. Sulphate and nitrate coatings function like a “focusing mirror”, thus light
438 absorption ability of the internally mixed soot particles are enhanced by 30% than soot alone (Fuller et al.,
439 1999). However, the BC concentration in foggy conditions was 6.12 µg m⁻³, and the absorption coefficient
440 is 143.7 Mm⁻¹, which were 2.09 and 0.83 times of the hazy days, respectively. The enhancement was much
441 greater than 30%. The reason is still not very clear and further investigation is thus needed. A variety of



442 metal particles were also observed in the foggy days, as foggy days had a stable low upper layer boundary
443 and slight wind, leading to the accumulation of pollutions. These pollution sources range from steel plants
444 and waste incineration to vehicle emission and so on (Hu et al., 2015).

445 **4 Conclusions**

446 Using the TEM and optical instruments, we investigated the particle morphological impact to the optical
447 properties by comparing the discrepancies during clear, haze and fog episodes in the summer of Beijing
448 unban. The clear episodes are most characterised by air mass from the north, which brings in slight mineral
449 particles. When a heavy rain occurred previously, it can washout the large particles and lower the particle
450 size distribution. Particle concentration was lower because most of particles existed in the form of external
451 mixture, leading to the attenuation of light absorption and scattering. Comparatively, haze and fog episodes
452 have higher particle concentration, larger size distribution and lower visibility. Pollutants such as metal
453 particles and fly ashes from the industries accumulate under the stagnated weather. In the later June, air
454 parcels from the intensive crop residue combustion region in the south introduce the biomass burning
455 emission, such as soot and K-rich particles, resulting in a period of severe haze. Light scattering and
456 absorption increase notably contributed by the mixed BC and other light absorption substances. In fog
457 periods, a large proportion of internally mixed particles, especially soot with the coating of nitrates or
458 sulphates, which favors the light absorption due to the “focusing mirror” effect. With the help of TEM, we
459 can directly investigate the size, mixing state, and chemical composition of the particles, thus provide
460 reference to the theoretical calculation of the BC model and ensure more precise interpretations of the
461 optical properties. However, the TEM analysis is done in the vacuum condition, which may cause the
462 decomposition and volatilization of some sensitive particles. Besides, the detail transition mechanism
463 among clear, haze and fog episodes needs higher time-resolved instrument and more statistics. All these
464 factors should be considered in the future studies.

465 **ACKNOWLEDGMENTS**



466 This work was supported by National Natural Science Foundation of China (Nos. 21577022, 21190053,
467 40975074), Ministry of Science and Technology of China (2016YFC0202700), and International
468 cooperation project of Shanghai municipal government (15520711200).

469 **References**

470 Adachi, K., and Buseck, P.: Internally mixed soot, sulfates, and organic matter in aerosol particles
471 from Mexico City, *Atmos. Chem. Phys.*, 8, 6469-6481, 2008.

472 Adler, G., Riziq, A. A., Erlick, C., and Rudich, Y.: Effect of intrinsic organic carbon on the optical
473 properties of fresh diesel soot, *P. Natl. Acad. Sci. USA.*, 107, 6699-6704, 2010.

474 Alexander, D. T., Crozier, P. A., and Anderson, J. R.: Brown carbon spheres in East Asian outflow
475 and their optical properties, *Science*, 321, 833-836, 2008.

476 Anderson, T. L., and Ogren, J. A.: Determining aerosol radiative properties using the TSI 3563
477 integrating nephelometer, *Aerosol Air Qual. Res.*, 29, 57-69, 1998.

478 Andreae, M., and Gelencsér, A.: Black carbon or brown carbon? The nature of light-absorbing
479 carbonaceous aerosols, *Atmos. Chem. Phys.*, 6, 3131-3148, 2006.

480 Bahadur, R., Praveen, P. S., Xu, Y., and Ramanathan, V.: Solar absorption by elemental and brown
481 carbon determined from spectral observations, *P. Natl. Acad. Sci. USA.*, 109, 17366-17371, 2012.

482 Bian, H., Chin, M., Rodriguez, J., Yu, H., Penner, J. E., and Strahan, S.: Sensitivity of aerosol
483 optical thickness and aerosol direct radiative effect to relative humidity, *Atmos. Chem. Phys.*, 9,
484 2375-2386, 2009.

485 Bond, T. C.: Spectral dependence of visible light absorption by carbonaceous particles emitted
486 from coal combustion, *Geophys. Res. Lett.*, 28, 4075-4078, 2001.

487 Buseck, P. R., and POsfai, M.: Airborne minerals and related aerosol particles: Effects on climate
488 and the environment, *P. Natl. Acad. Sci. USA.*, 96, 3372-3379, 1999.



489 Carabali, G., Mamani-Paco, R., Castro, T., Peralta, O., Herrera, E., and Trujillo, B.: Optical
490 properties, morphology and elemental composition of atmospheric particles at T1 supersite on
491 MILAGRO campaign, *Atmos. Chem. Phys.*, 12, 2747-2755, 2012.

492 Chakrabarty, R., Moosmüller, H., Chen, L.-W., Lewis, K., Arnott, W., Mazzoleni, C., Dubey, M.,
493 Wold, C., Hao, W., and Kreidenweis, S.: Brown carbon in tar balls from smoldering biomass
494 combustion, *Atmos. Chem. Phys.*, 10, 6363-6370, 2010.

495 Chameides, W. L., Yu, H., Liu, S., Bergin, M., Zhou, X., Mearns, L., Wang, G., Kiang, C., Saylor,
496 R., and Luo, C.: Case study of the effects of atmospheric aerosols and regional haze on agriculture:
497 An opportunity to enhance crop yields in China through emission controls?, *P. Natl. Acad. Sci.*
498 USA., 96, 13626-13633, 1999.

499 Charlson, R. J., Lovelock, J. E., Andreae, M. O., and Warren, S. G.: Oceanic phytoplankton,
500 atmospheric sulphur, cloud albedo and climate, *Nature*, 326, 655-661, 1987.

501 Che, H., Xia, X., Zhu, J., Li, Z., Dubovik, O., Holben, B., Goloub, P., Chen, H., Estelles, V., and
502 Cuevas-Agulló, E.: Column aerosol optical properties and aerosol radiative forcing during a
503 serious haze-fog month over North China Plain in 2013 based on ground-based sunphotometer
504 measurements, *Atmos. Chem. Phys.*, 14, 2125-2138, 2014.

505 China, S., Mazzoleni, C., Gorkowski, K., Aiken, A. C., and Dubey, M. K.: Morphology and mixing
506 state of individual freshly emitted wildfire carbonaceous particles, *Nature commun.*, 4, 2013.

507 Choël, M., Deboudt, K., Flament, P., Lecornet, G., Perdrix, E., and Sobanska, S.: Fast evolution
508 of tropospheric Pb-and Zn-rich particles in the vicinity of a lead smelter, *Atmos. Environ.*, 40,
509 4439-4449, 2006.



510 Chow, J. C., Bachmann, J. D., Wierman, S. S., Mathai, C., Malm, W. C., White, W. H., Mueller,
511 P. K., Kumar, N., and Watson, J. G.: Visibility: science and regulation, *J. Air. Waste Manage.*, 52,
512 973-999, 2002.

513 Clarke, A., McNaughton, C., Kapustin, V., Shinozuka, Y., Howell, S., Dibb, J., Zhou, J., Anderson,
514 B., Brekhovskikh, V., and Turner, H.: Biomass burning and pollution aerosol over North America:
515 Organic components and their influence on spectral optical properties and humidification response,
516 *J. Geophys. Res.-Atmos.*, 112, 2007.

517 Deng, X., Tie, X., Wu, D., Zhou, X., Bi, X., Tan, H., Li, F., and Jiang, C.: Long-term trend of
518 visibility and its characterizations in the Pearl River Delta (PRD) region, China, *Atmos. Environ.*,
519 42, 1424-1435, 2008.

520 Dey, S., Tripathi, S. N., Singh, R. P., and Holben, B. N.: Influence of dust storms on the aerosol
521 optical properties over the Indo-Gangetic basin, *J. Geophys. Res.-Atmos.*, 109,
522 10.1029/2004jd004924, 2004.

523 Doran, J., Barnard, J. C., Arnott, W., Cary, R., Coulter, R., Fast, J. D., Kassianov, E. I., Kleinman,
524 L., Laulainen, N. S., and Martin, T.: The T1-T2 study: evolution of aerosol properties downwind
525 of Mexico City, *Atmos. Chem. Phys.*, 7, 1585-1598, 2007.

526 Duan, F., Liu, X., Yu, T., and Cachier, H.: Identification and estimate of biomass burning
527 contribution to the urban aerosol organic carbon concentrations in Beijing, *Atmos. Environ.*, 38,
528 1275-1282, 2004.

529 Ebert, M., Weinbruch, S., Hoffmann, P., and Ortner, H. M.: The chemical composition and
530 complex refractive index of rural and urban influenced aerosols determined by individual particle
531 analysis, *Atmos. Environ.*, 38, 6531-6545, 2004.



532 Eck, T. F., Holben, B. N., Reid, J. S., Dubovik, O., Smirnov, A., O'Neill, N. T., Slutsker, I., and
533 Kinne, S.: Wavelength dependence of the optical depth of biomass burning, urban, and desert dust
534 aerosols, *J. Geophys. Res.-Atmos.*, 104, 31333-31349, 10.1029/1999jd900923, 1999.

535 Engling, G., Lee, J. J., Tsai, Y.-W., Lung, S.-C. C., Chou, C. C.-K., and Chan, C.-Y.: Size-resolved
536 anhydrosugar composition in smoke aerosol from controlled field burning of rice straw, *Aerosol*
537 *Air Qual. Res.*, 43, 662-672, 2009.

538 Fu, H., Zhang, M., Li, W., Chen, J., Wang, L., Quan, X., and Wang, W.: Morphology, composition
539 and mixing state of individual carbonaceous aerosol in urban Shanghai, *Atmos. Chem. Phys.*, 12,
540 693-707, 2012.

541 Fuller, K. A., Malm, W. C., and Kreidenweis, S. M.: Effects of mixing on extinction by
542 carbonaceous particles, *J. Geophys. Res.-Atmos.*, 104, 15941-15954, 1999.

543 Guo, L., Hu, Y., Hu, Q., Lin, J., Li, C., Chen, J., Li, L., and Fu, H.: Characteristics and chemical
544 compositions of particulate matter collected at the selected metro stations of Shanghai, China, *Sci.*
545 *Total Environ.*, 496, 443-452, 2014a.

546 Guo, Y., Feng, N., Christopher, S. A., Kang, P., Zhan, F. B., and Hong, S.: Satellite remote sensing
547 of fine particulate matter (PM_{2.5}) air quality over Beijing using MODIS, *Int. J. Remote Sens.*, 35,
548 6522-6544, 2014b.

549 Gustafsson, Ö., Kruså, M., Zenck, Z., Sheesley, R. J., Granat, L., Engström, E., Praveen, P., Rao,
550 P., Leck, C., and Rodhe, H.: Brown clouds over South Asia: biomass or fossil fuel combustion?,
551 *Science*, 323, 495-498, 2009.

552 Habib, G., Venkataraman, C., Bond, T. C., and Schauer, J. J.: Chemical, microphysical and optical
553 properties of primary particles from the combustion of biomass fuels, *Environ. Sci. Technol.*, 42,
554 8829-8834, 2008.



555 Hand, J. L., Malm, W., Laskin, A., Day, D., Lee, T.-b., Wang, C., Carrico, C., Carrillo, J., Cowin,
556 J. P., and Collett, J.: Optical, physical, and chemical properties of tar balls observed during the
557 Yosemite Aerosol Characterization Study, *J. Geophys. Res.-Atmos.*, 110, 2005.
558 Hansen, A.: The Aethalometer Manual, Magee Sci., Berkeley, Calif, 2003.
559 Hoffer, A., Gelencsér, A., Guyon, P., Kiss, G., Schmid, O., Frank, G., Artaxo, P., and Andreae,
560 M.: Optical properties of humic-like substances (HULIS) in biomass-burning aerosols, *Atmos.*
561 *Chem. Phys.*, 6, 3563-3570, 2006.
562 Hu, Y., Lin, J., Zhang, S., Kong, L., Fu, H., and Chen, J.: Identification of the typical metal
563 particles among haze, fog, and clear episodes in the Beijing atmosphere, *Sci. Total Environ.*, 511,
564 369-380, 2015.
565 Jacobson, M. Z.: Strong radiative heating due to the mixing state of black carbon in atmospheric
566 aerosols, *Nature*, 409, 695-697, 2001.
567 Jacobson, M. Z.: Control of fossil - fuel particulate black carbon and organic matter, possibly the
568 most effective method of slowing global warming, *J. Geophys. Res.-Atmos.*, 107, ACH 16-11-
569 ACH 16-22, 2002.
570 Jeong, C.-H., Hopke, P. K., Kim, E., and Lee, D.-W.: The comparison between thermal-optical
571 transmittance elemental carbon and Aethalometer black carbon measured at multiple monitoring
572 sites, *Atmos. Environ.*, 38, 5193-5204, 2004.
573 Kang, H., Zhu, B., Su, J., Wang, H., Zhang, Q., and Wang, F.: Analysis of a long-lasting haze
574 episode in Nanjing, China, *Atmos. Res.*, 120, 78-87, 2013.
575 Katrinak, K. A., Rez, P., Perkes, P. R., and Buseck, P. R.: Fractal geometry of carbonaceous
576 aggregates from an urban aerosol, *Environ. Sci. Technol.*, 27, 539-547, 1993.



577 Khoder, M.: Atmospheric conversion of sulfur dioxide to particulate sulfate and nitrogen dioxide
578 to particulate nitrate and gaseous nitric acid in an urban area, *Chemosphere*, 49, 675-684, 2002.

579 Kleinman, L. I., Daum, P. H., Lee, Y. N., Senum, G. I., Springston, S. R., Wang, J., Berkowitz, C.,
580 Hubbe, J., Zaveri, R. A., and Brechtel, F. J.: Aircraft observations of aerosol composition and
581 ageing in New England and Mid - Atlantic States during the summer 2002 New England Air
582 Quality Study field campaign, *J. Geophys. Res.-Atmos.*, 112, 2007.

583 Lack, D. A., Langridge, J. M., Bahreini, R., Cappa, C. D., Middlebrook, A. M., and Schwarz, J.
584 P.: Brown carbon and internal mixing in biomass burning particles, *P. Natl. Acad. Sci. USA.*, 109,
585 14802-14807, 10.1073/pnas.1206575109, 2012.

586 Langridge, J. M., Lack, D., Brock, C. A., Bahreini, R., Middlebrook, A. M., Neuman, J. A., Nowak,
587 J. B., Perring, A. E., Schwarz, J. P., and Spackman, J. R.: Evolution of aerosol properties impacting
588 visibility and direct climate forcing in an ammonia - rich urban environment, *J. Geophys. Res.-*
589 *Atmos.*, 117, 2012.

590 Lei, T., Zuend, A., Wang, W., Zhang, Y., and Ge, M.: Hygroscopicity of organic compounds from
591 biomass burning and their influence on the water uptake of mixed organic–ammonium sulfate
592 aerosols, *Atmos. Chem. Phys.*, 14, 11625-11663, 2014.

593 Lewis, K., Arnott, W. P., Moosmüller, H., and Wold, C. E.: Strong spectral variation of biomass
594 smoke light absorption and single scattering albedo observed with a novel dual - wavelength
595 photoacoustic instrument, *J. Geophys. Res.-Atmos.*, 113, 2008.

596 Li, C., Marufu, L. T., Dickerson, R. R., Li, Z., Wen, T., Wang, Y., Wang, P., Chen, H., and Stehr,
597 J. W.: In situ measurements of trace gases and aerosol optical properties at a rural site in northern
598 China during East Asian Study of Tropospheric Aerosols: An International Regional Experiment
599 2005, *J. Geophys. Res.-Atmos.*, 112, 2007.



600 Li, J., Pósfai, M., Hobbs, P. V., and Buseck, P. R.: Individual aerosol particles from biomass
601 burning in southern Africa: 2, Compositions and aging of inorganic particles, *J. Geophys. Res.-*
602 *Atmos.*, 108, 2003.

603 Li, W., and Shao, L.: Transmission electron microscopy study of aerosol particles from the brown
604 hazes in northern China, *J. Geophys. Res.-Atmos.*, 114, 2009.

605 Li, W., and Shao, L.: Direct observation of aerosol particles in aged agricultural biomass burning
606 plumes impacting urban atmospheres, *Atmos. Chem. Phys.*, 10, 10589-10623, 2010.

607 Li, W., Shao, L., and Buseck, P.: Haze types in Beijing and the influence of agricultural biomass
608 burning, *Atmos. Chem. Phys.*, 10, 8119-8130, 2010.

609 Moffet, R. C., Desyaterik, Y., Hopkins, R. J., Tivanski, A. V., Gilles, M. K., Wang, Y.,
610 Shuthanandan, V., Molina, L. T., Abraham, R. G., and Johnson, K. S.: Characterization of
611 aerosols containing Zn, Pb, and Cl from an industrial region of Mexico City, *Environ. Sci. Technol.*,
612 42, 7091-7097, 2008.

613 Moffet, R. C., and Prather, K. A.: In-situ measurements of the mixing state and optical properties
614 of soot with implications for radiative forcing estimates, *P. Natl. Acad. Sci. USA.*, 106, 11872-
615 11877, 2009.

616 Pathak, R. K., Yao, X., and Chan, C. K.: Sampling artifacts of acidity and ionic species in PM_{2.5},
617 *Environ. Sci. Technol.*, 38, 254-259, 2004.

618 Peppler, R., Bahrmann, C., Barnard, J. C., Laulainen, N., Turner, D., Campbell, J., Hlavka, D.,
619 Cheng, M., Ferrare, R., and Halthore, R.: ARM Southern Great Plains site observations of the
620 smoke pall associated with the 1998 Central American fires, *B. Am. Meteorol. Soc.*, 81, 2563-
621 2591, 2000.



622 Qian, Y., Wang, W., Leung, L. R., and Kaiser, D. P.: Variability of solar radiation under cloud -
623 free skies in China: The role of aerosols, *Geophys. Res. Lett.*, 34, 2007.

624 Quan, J., Zhang, Q., He, H., Liu, J., Huang, M., and Jin, H.: Analysis of the formation of fog and
625 haze in North China Plain (NCP), *Atmos. Chem. Phys.*, 11, 8205-8214, 2011.

626 Ram, K., Sarin, M., and Tripathi, S.: Temporal trends in atmospheric PM_{2.5}, PM₁₀, elemental
627 carbon, organic carbon, water-soluble organic carbon, and optical properties: impact of biomass
628 burning emissions in the Indo-Gangetic Plain, *Environ. Sci. Technol.*, 46, 686-695, 2012.

629 Ramana, M., Ramanathan, V., Feng, Y., Yoon, S., Kim, S., Carmichael, G., and Schauer, J.:
630 Warming influenced by the ratio of black carbon to sulphate and the black-carbon source, *Nat.*
631 *Geosci.*, 3, 542-545, 2010.

632 Ramanathan, V., Crutzen, P. J., Lelieveld, J., Mitra, A., Althausen, D., Anderson, J., Andreae, M.,
633 Cantrell, W., Cass, G., and Chung, C.: Indian Ocean Experiment: An integrated analysis of the
634 climate forcing and effects of the great Indo-Asian haze, 2001.

635 Ramanathan, V., Chung, C., Kim, D., Bettge, T., Buja, L., Kiehl, J., Washington, W., Fu, Q., Sikka,
636 D., and Wild, M.: Atmospheric brown clouds: Impacts on South Asian climate and hydrological
637 cycle, *P. Natl. Acad. Sci. USA.*, 102, 5326-5333, 2005.

638 Ramanathan, V., Ramana, M. V., Roberts, G., Kim, D., Corrigan, C., Chung, C., and Winker, D.:
639 Warming trends in Asia amplified by brown cloud solar absorption, *Nature*, 448, 575-578, 2007.

640 Roden, C. A., Bond, T. C., Conway, S., and Pinel, A. B. O.: Emission factors and real-time optical
641 properties of particles emitted from traditional wood burning cookstoves, *Environ. Sci. Technol.*,
642 40, 6750-6757, 2006.

643 Seinfeld, J. H., and Pandis, S. N.: *Atmospheric chemistry and physics: from air pollution to climate*
644 *change*, John Wiley & Sons, 2012.



645 Shi, Z., Shao, L., Jones, T. P., Whittaker, A., Lu, S., Berube, K. A., He, T., and Richards, R. J.:
646 Characterization of airborne individual particles collected in an urban area, a satellite city and a
647 clean air area in Beijing, 2001, *Atmos. Environ.*, 37, 4097-4108, 2003.
648 Solomon, S.: Climate change 2007-the physical science basis: Working group I contribution to the
649 fourth assessment report of the IPCC, Cambridge University Press, 2007.
650 Stanmore, B., Brilhac, J., and Gilot, P.: The oxidation of soot: a review of experiments,
651 mechanisms and models, *Carbon*, 39, 2247-2268, 2001.
652 Sun, Y., Zhuang, G., Tang, A., Wang, Y., and An, Z.: Chemical characteristics of PM2. 5 and
653 PM10 in haze-fog episodes in Beijing, *Environ. Sci. Technol.*, 40, 3148-3155, 2006.
654 Takemura, T., Nakajima, T., Dubovik, O., Holben, B. N., and Kinne, S.: Single-scattering albedo
655 and radiative forcing of various aerosol species with a global three-dimensional model, *J. Climate.*,
656 15, 333-352, 2002.
657 Wang, G., Kawamura, K., Xie, M., Hu, S., Cao, J., An, Z., Waston, J. G., and Chow, J. C.: Organic
658 molecular compositions and size distributions of Chinese summer and autumn aerosols from
659 Nanjing: Characteristic haze event caused by wheat straw burning, *Environ. Sci. Technol.*, 43,
660 6493-6499, 2009a.
661 Wang, H., He, C., Morawska, L., McGarry, P., and Johnson, G.: Ozone-initiated particle formation,
662 particle aging, and precursors in a laser printer, *Environ. Sci. Technol.*, 46, 704-712, 2012a.
663 Wang, R., Tao, S., Wang, W., Liu, J., Shen, H., Shen, G., Wang, B., Liu, X., Li, W., and Huang,
664 Y.: Black carbon emissions in China from 1949 to 2050, *Environ. Sci. Technol.*, 46, 7595-7603,
665 2012b.
666 Wang, X., and Chen, J.: Fog Formation in Cold Season in Ji’nan, China: Case Analyses
667 with Application of HYSPLIT Model, *Adv. Meteorol.*, 2014, 8, 10.1155/2014/940956, 2014.



668 Wang, X., Xu, B., and Ming, J.: An overview of the studies on black carbon and mineral dust
669 deposition in snow and ice cores in East Asia, *J. Meteorol. Res.*, 28, 354-370, 10.1007/s13351-
670 014-4005-7, 2014.

671 Wang, Y., Zhuang, G., Sun, Y., and An, Z.: The variation of characteristics and formation
672 mechanisms of aerosols in dust, haze, and clear days in Beijing, *Atmos. Environ.*, 40, 6579-6591,
673 2006.

674 Wang, Y., Che, H., Ma, J., Wang, Q., Shi, G., Chen, H., Goloub, P., and Hao, X.: Aerosol radiative
675 forcing under clear, hazy, foggy, and dusty weather conditions over Beijing, China, *Geophys. Res.*
676 *Lett.*, 36, 2009b.

677 Wu, D., Mao, J., Deng, X., Tie, X., Zhang, Y., Zeng, L., Li, F., Tan, H., Bi, X., and Huang, X.:
678 Black carbon aerosols and their radiative properties in the Pearl River Delta region, *Science in
679 China Series D: Earth Sciences*, 52, 1152-1163, 2009.

680 Xia, X., Chen, H., Wang, P., Zhang, W., Goloub, P., Chatenet, B., Eck, T., and Holben, B.:
681 Variation of column - integrated aerosol properties in a Chinese urban region, *J. Geophys. Res.-
682 Atmos.*, 111, 2006.

683 Yan, P., Tang, J., Huang, J., Mao, J., Zhou, X., Liu, Q., Wang, Z., and Zhou, H.: The measurement
684 of aerosol optical properties at a rural site in Northern China, *Atmos. Chem. Phys.*, 8, 2229-2242,
685 2008.

686 Yang, M., Howell, S., Zhuang, J., and Huebert, B.: Attribution of aerosol light absorption to black
687 carbon, brown carbon, and dust in China–interpretations of atmospheric measurements during
688 EAST-AIRE, *Atmos. Chem. Phys.*, 9, 2035-2050, 2009.

689 Yu, X., Cheng, T., Chen, J., and Liu, Y.: A comparison of dust properties between China continent
690 and Korea, Japan in East Asia, *Atmos. Environ.*, 40, 5787-5797, 2006.



691 Zhang, R., Khalizov, A. F., Pagels, J., Zhang, D., Xue, H., and McMurry, P. H.: Variability in
692 morphology, hygroscopicity, and optical properties of soot aerosols during atmospheric processing,
693 P. Natl. Acad. Sci. USA., 105, 10291-10296, 2008.

694 Zhang, W., Zhuang, G., Guo, J., Xu, D., Wang, W., Baumgardner, D., Wu, Z., and Yang, W.:
695 Sources of aerosol as determined from elemental composition and size distributions in Beijing,
696 Atmos. Res., 95, 197-209, <http://dx.doi.org/10.1016/j.atmosres.2009.09.017>, 2010.

697

698

699



700 **Table 1** Details about the analysed samples on the sampling time, instantaneous meteorological state and
701 the number of particle analysed in each sample.

Date	Sampling Time (BST ^a)			Conditions	RH (%)	Temp. (°C)	Wind		Visibility (km)	No.
	Starting	Duration					Speed (m/s)	Direction		
25-05-2012	13:40	4 min	Clear	20	29	2	160	-	136	
30-05-2012	9:31	16 min	Clear	29	24	7	350	-	92	
02-06-2012	9:00	1 min	Mist ^b	83	20	4	180	2	146	
02-06-2012	13:27	2 min	Clear	48	27	4	190	-	138	
03-06-2012	10:13	15 s	Fog	88	22	1	variable	1.2	110	
18-06-2012	18:52	2 min	Haze	55	29	3	140	3	172	
19-06-2012	9:10	2 min	Haze	61	25	1	variable	2.8	120	
21-06-2012	9:10	1 min	Haze	69	26	2	110	2.2	117	
23-06-2012	12:45	2 min	Mist ^b	84	25	4	120	3	142	

^aBeijing standard time (8 h prior to GMT).

^bMist is studied here as fog.



704 **Figure captions**

705 **Figure 1.** 5 episodes categorization. EP-1 features haze induced mainly from transportation of south
706 industrial pollution, EP-2 clear, EP-3 frequent transition among haze, fog and clear conditions, EP-4 clear
707 with rain interrupted, and EP-5 haze resulted mainly from the biomass burning.

708 **Figure 2.** The 3-day back-trajectory clusters of each episode, arriving at Beijing at the height of 100 m,
709 together with the fire spot distribution of these periods.

710 **Figure 3.** TEM typical views of the particles in clear (upper panel), haze (middle panel) and fog episodes
711 (bottom panel). 9 components are marked with the colourful arrows. (a1) (b1) (c1) (d1) (e1) (f1) is obtained
712 before the electron exposure and (a2) (b2) (c2) (d2) (e2) (f2) is after exposure. A fraction of S-rich particles
713 and other unstable particles decompose after electron exposure.

714 **Figure 4.** 9 categories of particles under the TEM view. The inserted spectra are obtained by the EDS, and
715 the grid like images are acquired from the SAED. (a) S-rich, (b) N-rich, (c) mineral, (d) K-rich, (e) soot, (f) tar
716 ball, (g) organic, (h) metal, (i) fly ash.

717 **Figure 5.** Variation of optical parameters during the study period. (a) Total Aerosol optical depth (AOD),
718 and AOD resulted from Mie scatter and Rayleigh scatter; (b) Ångström exponent (\AA) computed from the
719 pairs of 700 nm and 450 nm, 700 nm and 550 nm, and 550 nm and 450 nm; (c) light extinction, absorption
720 and scattering coefficients; (d) calculated single scattering albedo (SSA).

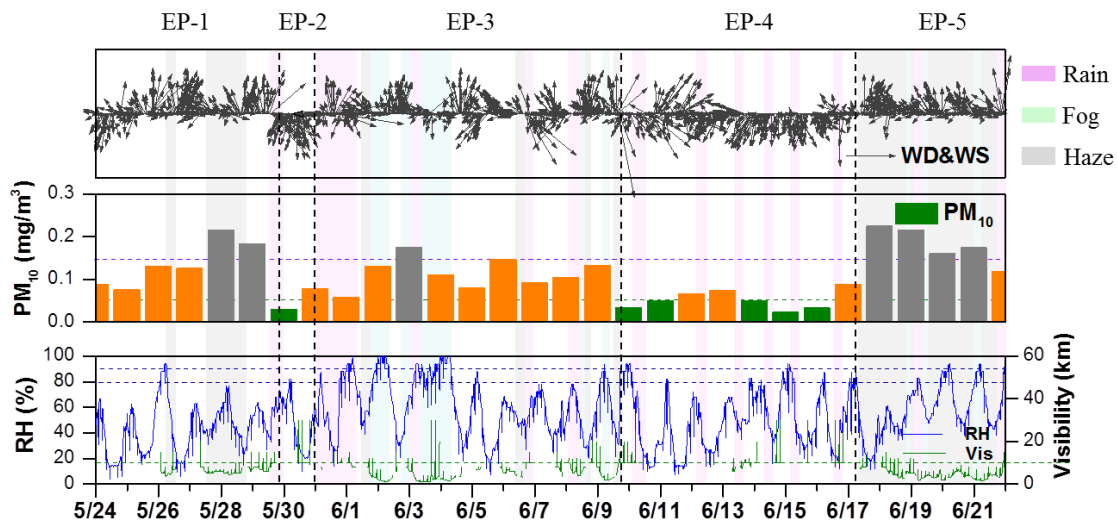
721 **Figure 6.** Percentages of 9 particle components under clear, haze and fog conditions with different mixing
722 states.

723 **Figure 7.** BC concentrations converted from the data measured by AE-31 and MAAP. Good correlation is
724 observed.

725



726



727

728

729

730

731

732

733

734

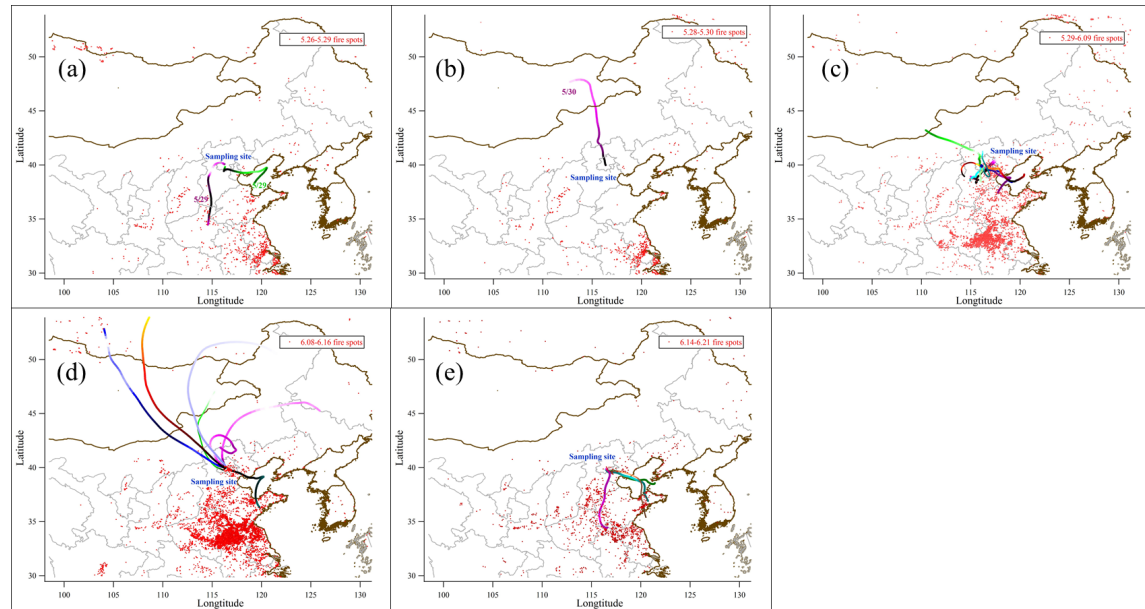
735

736

737

738

Figure 1



739

740

741

742

743

744

745

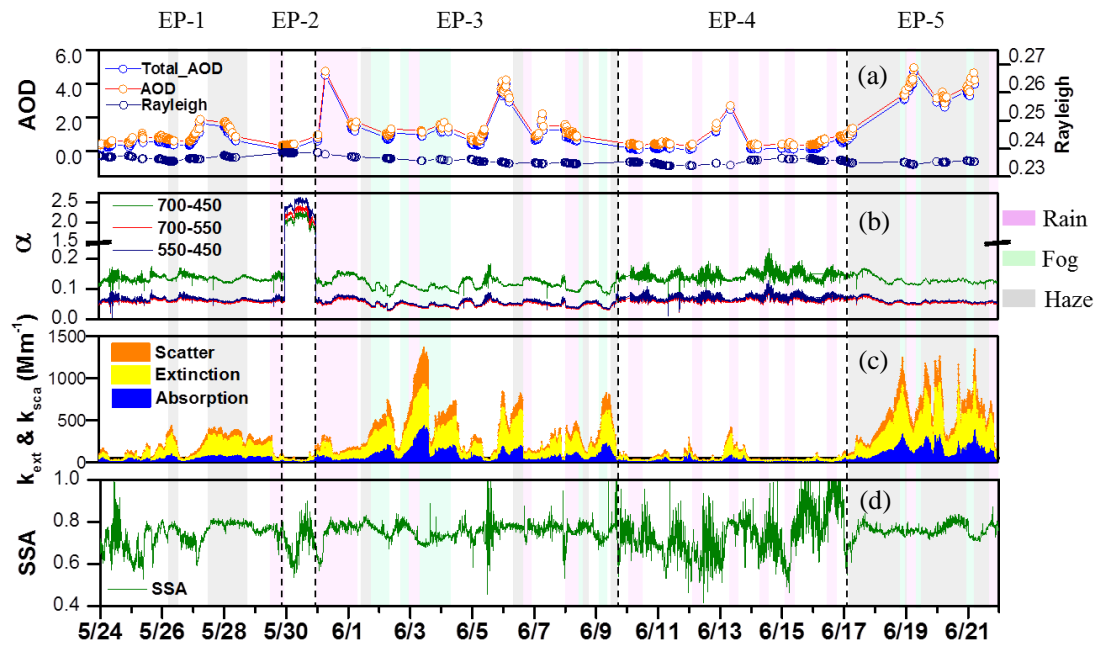
746

Figure 2



747

748



749

750

751

752

753

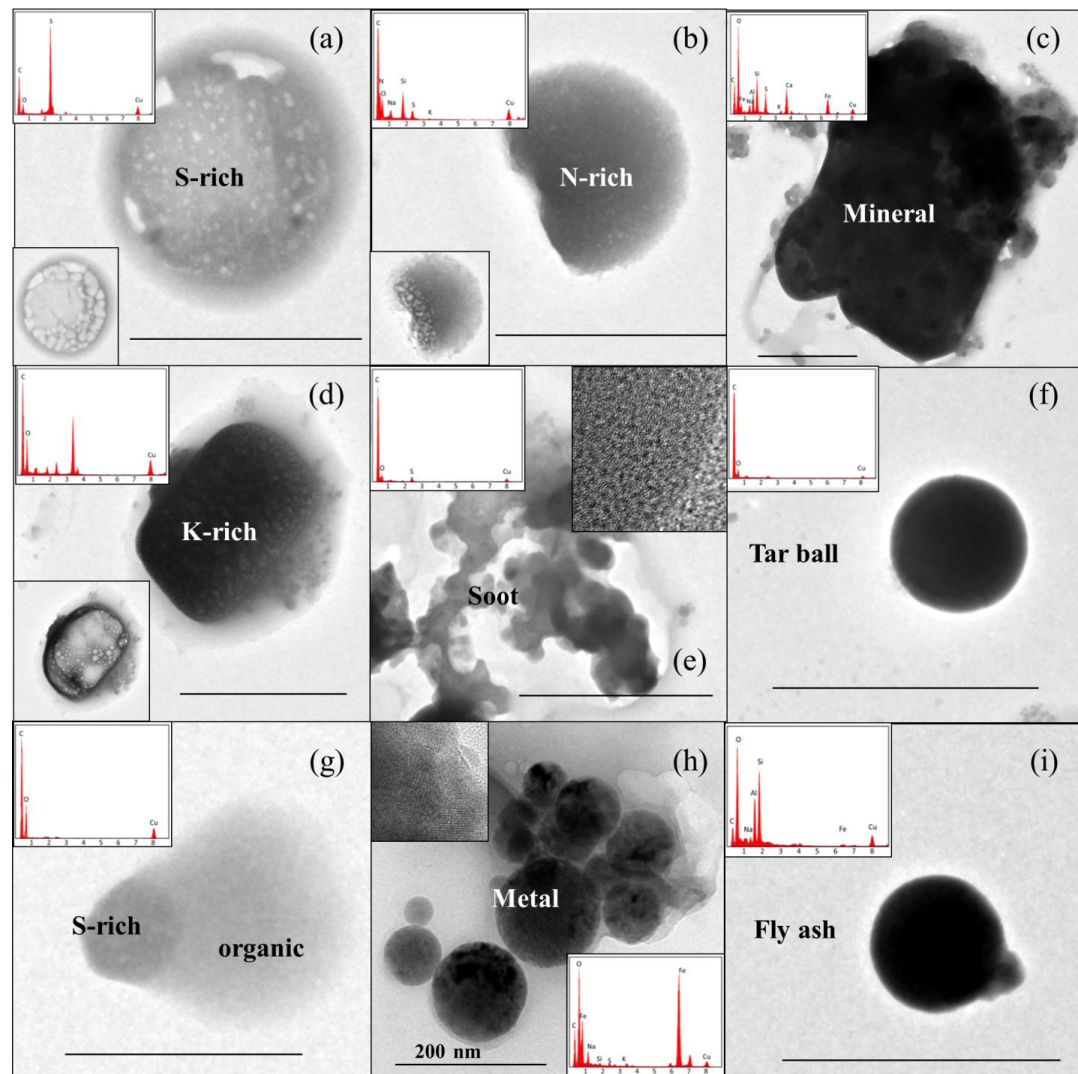
754

755

Figure 3



756



757

758

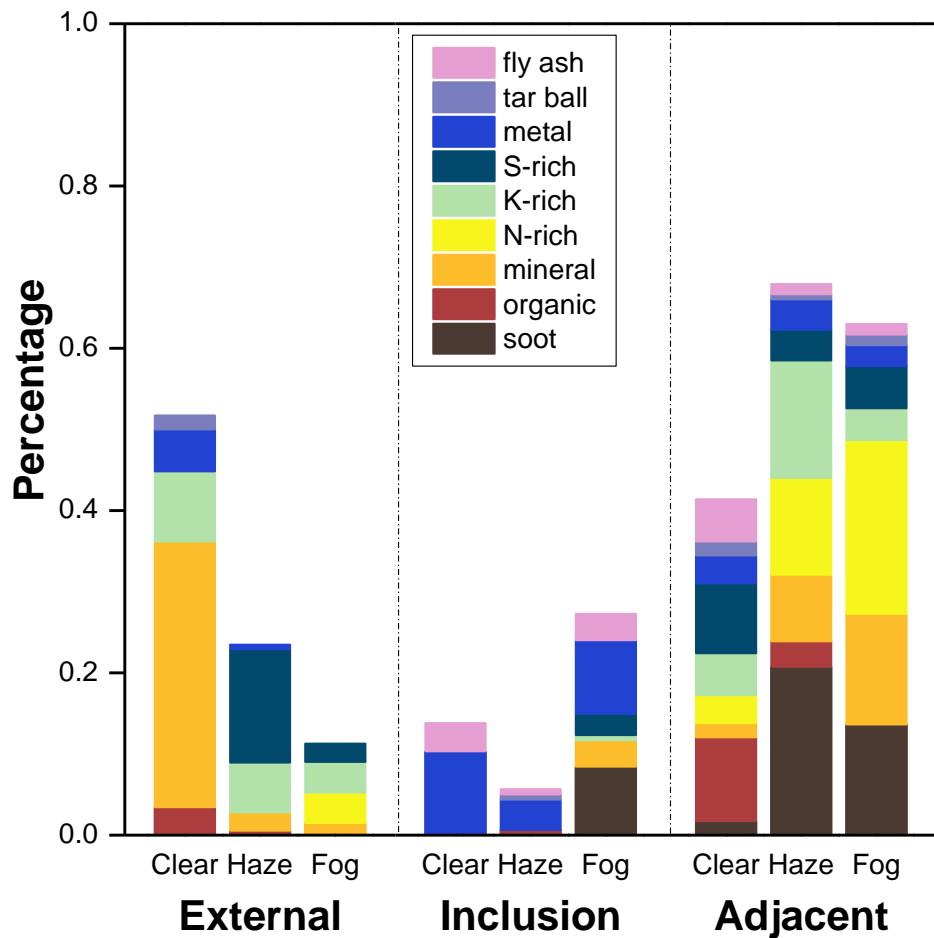
759

760

761

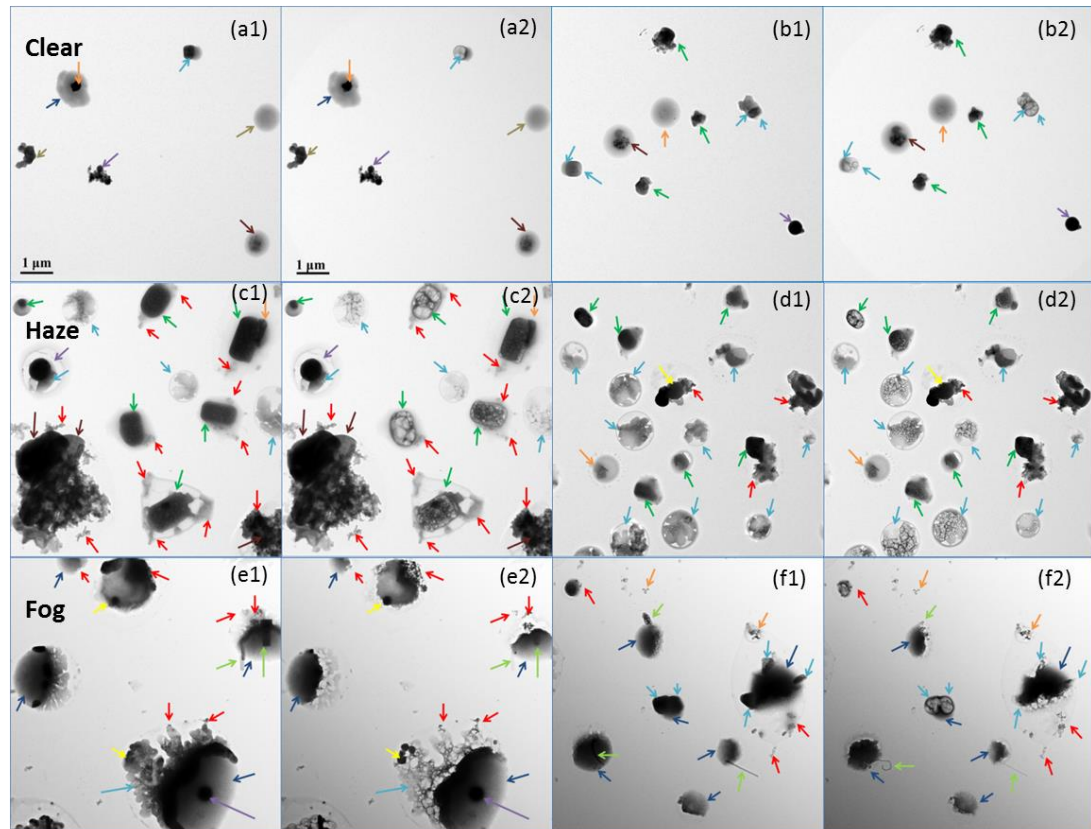
762

Figure 4



763
764
765
766

Figure 5



K-rich → S-rich → soot → fly ash → metal →
 Ca-S → tar ball → N-rich → rod → organic →

767

768

769

770

771

772

Figure 6

